Non-contact measurement of neck pulses achieved by imaging micro-motions in the neck skin

QINGHUA HE,[1,2,†] Wenqian Geng,[2,3,†] Wanyu Li,[2,3] AND Ruikang K. Wang[1,2,3,*]

[1]*Department of Bioengineering, University of Washington, Seattle, WA 98105, USA*
[2]*Department of Ophthalmology, University of Washington, Seattle, WA 98105, USA*
[3]*Department of Hepatobiliary and Pancreatic Medicine, The first Hospital of Jilin University NO.71 Xinmin Street, Changchun, Jilin 130021, China*
[†]These authors contributed equally to this work
[*]*wangrk@uw.edu*

Abstract: We report a method and system of micro-motion imaging (µMI) to realize non-contact measurement of neck pulses. The system employs a 16-bit camera to acquire videos of the neck skin, containing reflectance variation caused by the neck pulses. Regional amplitudes and phases of pulse-induced reflection variation are then obtained by applying a lock-in amplification algorithm to the acquired videos. Composite masks are then generated using the raw frame, amplitude and phase maps, which are then used to guide the extraction of carotid pulse (CP) and jugular vein pulse (JVP) waveforms. Experimental results sufficiently demonstrate the feasibility of our method to extract CP and JVP waves. Compared with conventional methods, the proposed strategy works in a non-contact, non-invasive and self-guidance manner without a need for manual identification to operate, which is important for patient compliance and measurement objectivity. Considering the close relationship between neck pulses and cardiovascular diseases, for example, CA stenosis, the proposed µMI system and method may be useful in the development of early screening tools for potential cardiovascular diseases.

1. Introduction

Cardiovascular diseases lead to millions of deaths worldwide each year, giving rise to a heavy social burden due to its high morbidity and mortality [1,2]. Numerous methods, such as computed tomography angiography and cardiovascular magnetic resonance imaging, have been developed in response to fighting cardiovascular diseases, aiming for diagnosis, monitoring and treatment management [3–6]. However, let alone their high cost, these devices require special and dedicated expertise to properly operate, which somehow prevents them from being accessible by the public and even nonprofessionals. Currently, the lack of accessible diagnostic and monitoring tools is largely responsible for the slow development of possible effective screening methods for this disease. To meet this challenge, researchers have made good attempts to develop camera-enabled skin imaging methods, including thermal imaging [7–9], autofluorescence imaging [10,11], hemodynamics imaging [12–14] and laser speckle imaging methods [15,16] to assess the cardiovascular functions. However, the derived signals from the body-skin surface in these methods are highly dependent on cutaneous tissue structures, capillary beds, and pigment features, which can affect their accuracy to predict dysfunctions in large blood vessels and hearts. Therefore, there is a demand to develop more cost-effective techniques that can directly reflect the health status of the cardiovascular system.

Following the contraction and relaxation of each heart cycle, a pressure wave would be generated that propagates through the body via blood vessels. When it passes across the carotid artery (CA) and the jugular vein (JV), it causes the blood flow volume in them to show pulsatile

variations, producing carotid pulse (CP) and JV pulse (JVP) waves [17,18]. A CP waveform usually consists of a forward wave and a reflective wave, whereas a typical JVP waveform shows three positive deflections, "a", "c" and "v" waves, and two descents, "x" and "y" waves [19,20]. These sub-waves are closely related to cardiac cycle and blood flow conditions, thus may be leveraged for clinical use in the monitoring and even prediction of cardiac and cardiovascular abnormalities [21–23]. As a result, accurate measurements of CP and JVP waveforms would be of clinical interest in both the assessment and the screening of cardiovascular diseases.

In response to this clinical interest, researchers have attempted a number of methods to assess the CP and JVP waveform, including both invasive and non-invasive strategies. For example, central venous catheterization is used to measure JVP waveform by inserting a catheter into JVs [24]. This invasive method is currently the gold standard in clinics but requires surgical expertise and often causes pain to patients. Doppler ultrasound imaging is another commonly used tool for the measurement of pulse waves from the CA and JV [25,26]. However, Doppler ultrasound imaging requires both expensive devices and well-trained operators. Recently, photoplethysmography (PPG) technique has been applied to provide pulse waveform by placing an optical sensor on the skin regions of interest (ROI), overlaying the underneath arteries or veins [27–30]. The blood pulsation in these large vessels gives rise to variations of light absorption, thus can be detected by an optical sensor. Nevertheless, a typical PPG device works in a contact mode. In addition to the possible discomfort to patients, it requires accurate positioning to guide the extraction of pulse waveform from the measurements. This guidance is usually provided by additional technique and hardware, unavoidably increasing the complexity in measurements [31].

In this paper, we propose a camera-based micro-motion imaging (μMI) method to image regional motions of neck skin to enable a non-contact measurement of CP and JVP waves. Blood pulsation in large vessels introduces periodical pressures to the surrounding tissue. Due to relatively stronger pulses and more superficial positions of common CA and JV, the pressure waves generated by the CP and JVP pulsation located within the neck skin tissue beds can propagate to the skin surface, leading to relatively larger surface motion at the regions overlying these vessels than other regions. In our method, we record videos of the light reflectance from the skin surface located at the neck region to capture the tissue micro-motions, upon which to extract their blood-pulsation-related components with lock-in amplification algorithm. Since the blood pulsations in arteries and veins vary in phases and amplitudes (strengths), the generated tissue motions are assumed to show regional diversity as well. To mitigate this complication, we create composite masks by combining the raw signal strength with amplitude and phase signals together. The waveforms of CP and JVP are then regionally extracted under the guidance of these masks for more accurate assessments. Our study presents the μMI approach for capturing tissue motions in the CA and JV at the neck region. Unlike previous techniques, μMI directly accesses CA and JV information, simplifying cardiovascular function assessment. By utilizing a composite mask, our approach automatically identifies regions of interests that represent CP and JVP. Importantly, μMI eliminates the need for manual identification of pulsation regions, minimizing the subjectiveness in measurements.

2. Methods and materials

2.1. Experimental setup

The schematic setup of the proposed μMI system is illustrated in Fig. 1(a), where the neck skin was illuminated by a ring LED white light and then imaged by a 16-bit-depth camera (Chronos 1.4, Kron Technologies Inc. Canada). The spectral power density of the ring LED light source is shown in Fig. 1(b). The relative spectral sensitivities of the R, G and B channels in the camera are shown in Fig. 1(c). The ring LED provided uniform illumination in the field of view, where the values of U1 and U2 (the metrics used to assess irradiance uniformity [31]) were measured to be 0.99 and 0.96, respectively. The reason for the selection of a 16-bit-depth camera in the

setup was to ensure that the camera sensor can record pulsatile signals with higher fidelity. This is important because the motion induced reflectance change only represents a small fraction of the background reflectance. The change of reflection caused by neck pulsatile motions, mixed with signals from respiration motion, global motion and blood absorption signals, are recorded together in videos for further processing.
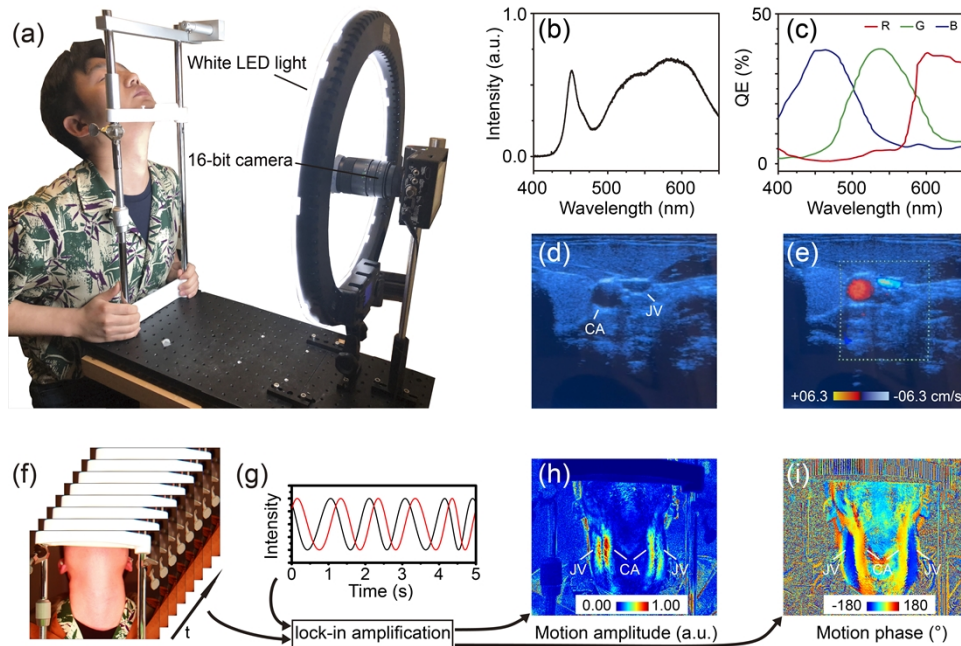

Fig. 1. (a) Photograph of μMI system setup. (b) Spectral power density of the white ring LED light source used for illumination. (c) Relative spectral sensitivities of R, G and B channels in the camera. (d) Ultrasound and (e) color Doppler ultrasound imaging of the left-side carotid artery (CA) and jugular vein (JV). A recorded video of color Doppler ultrasound imaging is provided in the supplementary material for the confirmation of the blood pulsations in CA and JV [see **Visualization 1**]. (f-j) Schematic of processing with lock-in amplification algorithm: (f) Video of neck skin after motion correction. (g) Reference function. (h) Amplitude map of heart-cycle-related micro-motion. (i) Phase map of heart-cycle-related micro-motion.

2.2.   Video acquisition

Healthy volunteers were enrolled in this study to investigate the performance of the μMI method. This study adhered to tenets of the Declaration of Helsinki and was performed in accordance with the Health Insurance Portability and Accountability Act. Ethical approval was obtained from the Institutional Review Board of the University of Washington. Informed consent was obtained from the subject prior to the start of each study session.

Before imaging, the volunteer was asked to sit in a chair for five minutes to stabilize the heart cycle. Then, the volunteer was asked to place his/her jaw on the chin rest to expose neck skin for video recording. During camera imaging, precautions were taken to ensure stability and minimize motion artifacts. Subjects were instructed to avoid large body movements, deep breaths, and swallowing, in order to record a stable video. The video recording lasted for 10 seconds at 100 frames per second. The pixel resolution of each frame was set to be 640×512.

To confirm the pulsatile blood flow in both CA and JV at this sitting position, we used a clinical Doppler ultrasound machine (EUB-8500, Hitachi Medical Co.) to image dynamic blood flow information. Figure 1(d) shows the ultrasound anatomy of the left-side neck at this position. The corresponding color Doppler ultrasound image (Fig. 1(e)) confirms that 1) the pulsatile blood flow exists not only in the carotid artery, but also in the jugular vein; and 2) the blood flow direction in the CA is opposite to that in JV, which is expected.

2.3. Calculation of amplitude and phase map

As stated earlier, the recorded video contains signals caused by various motions and optical property of the skin tissue beds of interest, including blood absorption. To extract neck pulse waveform, we need to purify the video signals by filtering out other signal components to retain the pulse-enabled micro-motions. For this purpose, we first applied a subpixel registration algorithm to correct global motions caused by the instability of the system. Considering that pulse-induced micro-motions only exist in localized skin regions, it is important to guide the selection of target regions for accurate extraction of the neck pulse waveform. For doing so, we applied a lock-in amplification algorithm to calculate the pulsation maps from the video signals. The details of the algorithm can be found in a previous study [31]. Briefly, we first extracted pulsatile signals from the video sequence (Fig. 1(f)) by filtering out other motion components to only retain the signals with heartbeat frequencies. The resulting signal (Fig. 1(g)) was used as a reference function to extract and amplify the localized pulsatile signal with the same frequency component as in the reference function at each voxel of the video. This processing procedure resulted in amplitude and phase maps, shown in Figs. 1(h) and (i), respectively. Note that these maps also include signals from blood absorption, which fluctuates at heart rate frequencies as well, thus cannot be eliminated. However, in the next part, we demonstrated that by comparing with the motion-induced signal pulsation, the absorption-induced pulsation is much weaker, thus may be neglected from the results.

2.4. Complexity of pulses in neck skin

The motion within the neck skin reflects multiple types of pulsations, including CP, JVP, respiration and blood pulsation in capillaries, complicating the extraction of CP and JVP waveforms. To show the complication, we selected different regions of the neck skin and extracted their pulse waveforms from the video (Fig. 2). Figure 2(a) shows the regions of interest, including two linear horizontal profiles located at the jaw and neck regions, and seven sampling positions in the neck area. The position selection is illustrated below.

It is reasonable to assume that at the skin tissue beds located under the jaw, the profile would be dominated by the blood absorption because of the lack of large blood vessels in the region. However, at the neck skin region, the profile would be modulated by the motion-induced pulsation due to the existence of the CV and JVP directly beneath the skin tissue beds. Figure 2(b) compares the temporal-spatial fluctuation amplitude maps of the linear profiles at the jaw and neck skin regions, respectively, where they show that the fluctuation amplitudes at the jaw skin region are much weaker than those at the neck skin region, suggesting that blood pulsation due to absorption may be negligible when extracting micro motion pulses. Besides, the temporal-spatial amplitude map of neck skin shows distinct periodic types of fluctuations, with varied frequencies at different spatial positions. To investigate this further, we extracted the temporal signals at the positions with observable periodic signals (7 positions as shown in Fig. 2(a)).

According to anatomy, we expect that JVP and CP waveforms would dominate the neck region. However, the extracted waveforms from sampling positions (Fig. 2(c)) show higher complexity. Specifically, the waveform of the position 4 exhibits a lower frequency ($\sim$0.47 Hz) than the heart rate ($\sim$1.20 Hz), while at the positions 1 and 7 there appear weaker pulsation amplitudes and more indistinguishable pulse waveforms than what we would expect from CP and JVP.
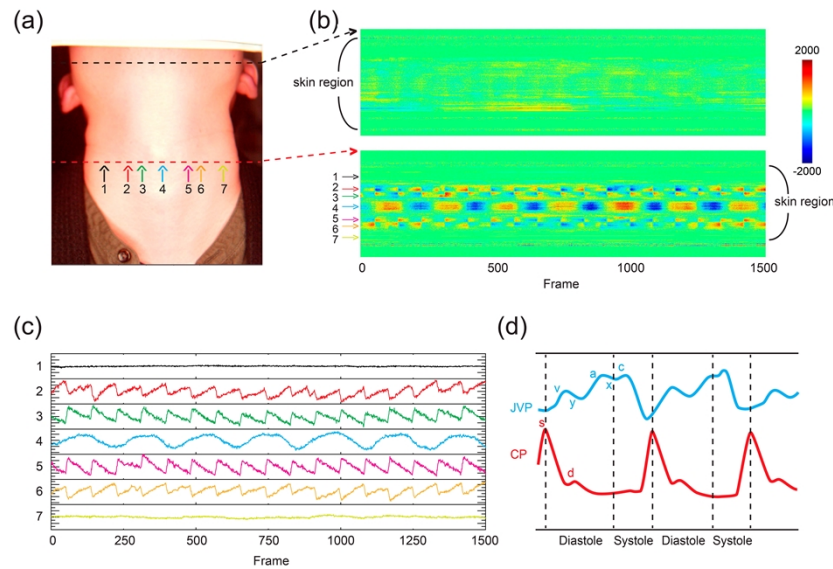
Fig. 2. Illustration of potential challenges in extracting pulse signals from video of neck skin. (a) The locations of two linear pixel profiles in the jaw and neck areas, respectively, as well as seven sampling positions in the neck area. The sampling positions were positioned according to the pulsation amplitude types in (b). (b) Temporal-spatial fluctuation maps obtained at the linear spatial profiles located at the jaw (top line in (a)) and neck regions (bottom line in (a)), respectively. (c) The detrended pulse waves extracted from the seven positions labeled in (a) and (b). (d) The typical CP and JVP waveforms, with labels "a, c, v, x, y, s, d" as described in the accompanying text.

Theoretically, CP and JVP pulses contain some typical features that can be used to estimate cardiovascular functions [30]. As shown in Fig. 2(d), the typical CP waveform includes a systolic part "s", which mainly arises from a forward pressure wave, and a diastolic component "d", which arises from reflected pressure waves in the common CA. The JVP waveform includes similar components like positive "a", "c", "v" waves that respectively arise from atrial contraction, ventricular contraction and atrial venous filling, and negative "x", "y" waves from atrial relaxation and ventricular filling, respectively. Furthermore, the CP and JVP waves propagate in opposite directions, i.e. they are in the reversed phase. However, the features of the JVP and CP waveform were not observed in the waveforms at some positions. These results indicate that there are diverse pulse waveforms in the neck skin, thus, guidance is necessary in order to extract the neck pulse waveforms of interest.

2.5. Generation of composite masks

From the motion amplitude map in Fig. 1(h), there appear four distinct linear regions with high motion amplitudes (roughly appearing in the middle of the image), located at the two sides of the neck. With reference to anatomy, we reasoned these signals (from left to right) should be caused by pulses from right JV, right CA, left CA and left JV, respectively. As shown in the phase map in Fig. 1(i), the two regions covering arteries appear to have a delayed phase, whereas the other two regions covering veins appear to have a leading phase. This indicates that pulsations between CP and JVP waves are in an opposite phase relationship. To extract the pulsatile waveform more accurately, we decided to utilize these features to create composite masks as the guidance for pulse extraction. In the specific operation, the composite mask was generated by a product between three independent masks, including the skin mask, amplitude mask and phase mask.

2.6. Skin mask

To exclude non-skin regions, we first created a binary mask, M_{skin}, from the green channel in raw image by setting a fixed threshold of 20% full-well capacity of the camera (Fig. 3(a)). However, exceptions may exist, like light colored clothes and decorative wearables that the subject wears. In this case, some precautions should be taken to eliminate these exceptions to produce a correct mask.
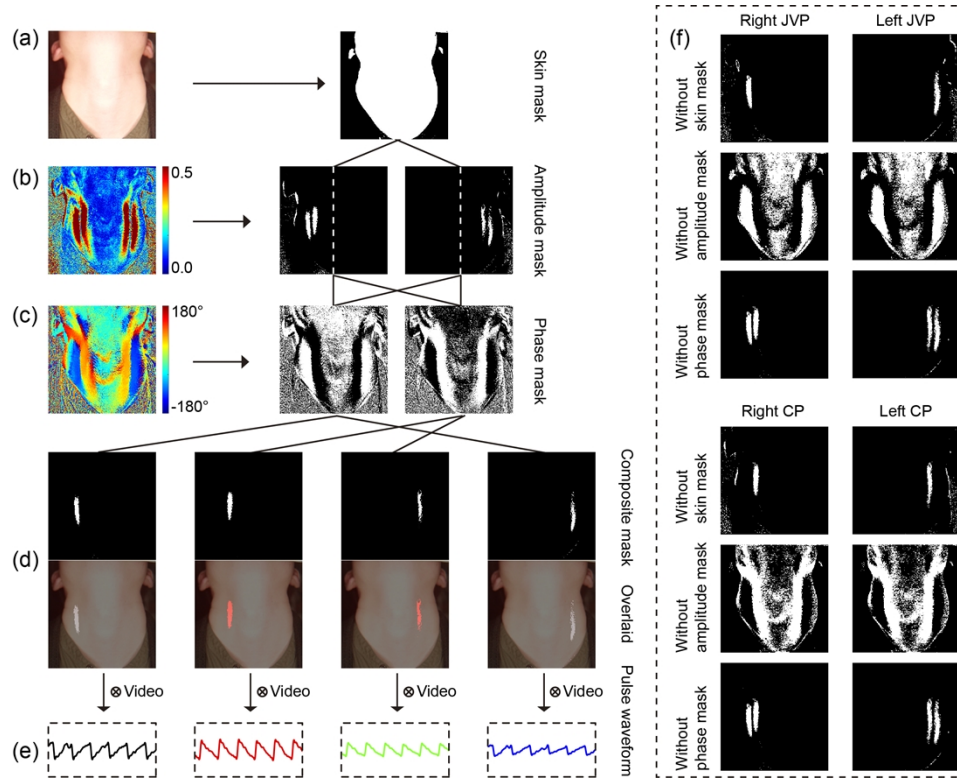

Fig. 3. Generation of composite masks to guide the extraction of the CP and CVP waveforms. (a) Generation of the skin mask from the green channel of RGB frames. Binary mask was created by setting up an intensity threshold of 20% full-well capacity of the camera to exclude background signals. (b) Generation of amplitude masks. A binary mask was first generated by thresholding the image at 50% maximum value. Two separate masks were then produced to represent regions of the left and right neck by splitting the binary mask with a reference to Adam's apple. (c) Generation of the phase masks, where two binary masks were produced by simply selecting the pixels with positive and negative phase values, respectively. (d) Generation of the composite masks. Four composite masks were created by performing the dot products of skin, amplitude and phase mask masks as described in Section 2.5. (e) Extraction of the neck pulse by applying composite masks to skin videos and calculating the temporal variation of the average value of masked regions in each frame. (f) Evaluation of the contribution of each mask to the composite mask. The masks for four target regions were generated by removing each skin, amplitude, and phase masks, respectively.

2.7. Amplitude mask

Since strong pulsatile blood flow exists in JV and CA, the induced pressure would cause stronger periodical motion on target regions than the surrounding skin regions. To select these targeted

regions, we calculated binary amplitude masks, M_{amp}, from the amplitude map by simply selecting the pixels with motion amplitude values higher than the default threshold (half the maximum value within the skin mask region). Figure 3(b) shows four distinct linear regions were kept within the mask. To separate signals between the left and right sides of the neck, two independent unilateral masks, M_L and M_R, were produced simply by splitting the mask into two halves with a reference to Adam's apple.

2.8. Phase mask

As we stated above, blood flows in JV and CA should be approximately in reversed phases. Therefore, by selecting the pixels with negative and positive phase values, we created two binary masks for JVP and CP, respectively (Fig. 3(c)). We refer these two masks to M_{neg} and M_{pos}, respectively.

2.9. Composite mask

Finally, the composite masks were generated by a product operation among the three masks produced above to identify the regions that represent the right JVP, right CP, left JVP and left CP, respectively:

$$M_{right\ JVP} = M_{skin} \otimes M_{amp} \otimes M_R \otimes M_{neg}$$

$$M_{right\ CP} = M_{skin} \otimes M_{amp} \otimes M_R \otimes M_{pos}$$

$$M_{Left\ CP} = M_{skin} \otimes M_{amp} \otimes M_L \otimes M_{neg}$$

$$M_{Left\ JVP} = M_{skin} \otimes M_{amp} \otimes M_L \otimes M_{pos}$$

where $\otimes$ denotes dot product. This product operation enables the exclusion of non-skin background regions, non-CA/JV skin regions, and edges from the images, as shown in Fig. 3(d). Additionally, the CA and JV regions on both sides of the neck skin can be separated.

Finally, the pulse waveforms from the CA and JVP are obtained by multiplying these masks with the time series of frames in videos. With these steps, the resulting pulse waveforms for the right JVP, right CA, left CA and left JVP are shown in Fig. 3(e), respectively.

To assess the contribution of each mask in the final composite mask, we conducted an ablation experiment by removing each one of the masks individually in the whole processing. Figure 3(f) illustrates the resulting masks of four regions when excluding the skin, amplitude, and phase masks, respectively. Firstly, without the skin mask, we can observe that some background noise would present in the resulting masks. This indicates that skin masks play a crucial role in removing unwanted signals and noise from the measurement. When the amplitude mask was removed, we can see that not only the CP and JVP regions but also other skin regions would result, leading to the unexpected inclusion of blood absorption and respiration signals, which may distort the accuracy of the extracted waveforms. Furthermore, when the phase masks were excluded from the composite mask, the generated result displays two regions, indicating that the CP and JVP regions have not been properly separated, resulting in a mixture of CP and JVP waveforms. This lack of separation can significantly affect the reliability and interpretability of the extracted waveforms. Overall, the ablation experiment highlights the importance of including all the components, i.e., the skin, amplitude, and phase masks, in the composite mask to ensure accurate and reliable extraction of CP and JVP waveforms.

3. Results

Nine volunteers (age = 29.2 ± 2.5 years old, five males and four females) were recruited and imaged and we show three of them as examples in Fig. 4. The CP and JVP waveforms from each subject (plots shown in the right part of the Fig. 4) were extracted from the videos under the guidance of composite masks. In doing so, we recorded the videos for 10s from which CP and

JVP waveforms were extracted according to the procedures described above. Although the pulse waveforms of different subjects may display varying shapes, the right and left carotid pulses demonstrate distinct systolic peaks and dicrotic notches. Additionally, the majority of jugular venous pressure (JVP) curves exhibit the aforementioned characteristic three positive and two negative waves. These extracted waveforms and features provide visual evidence for the potential of our measurements to be applied on different individuals.
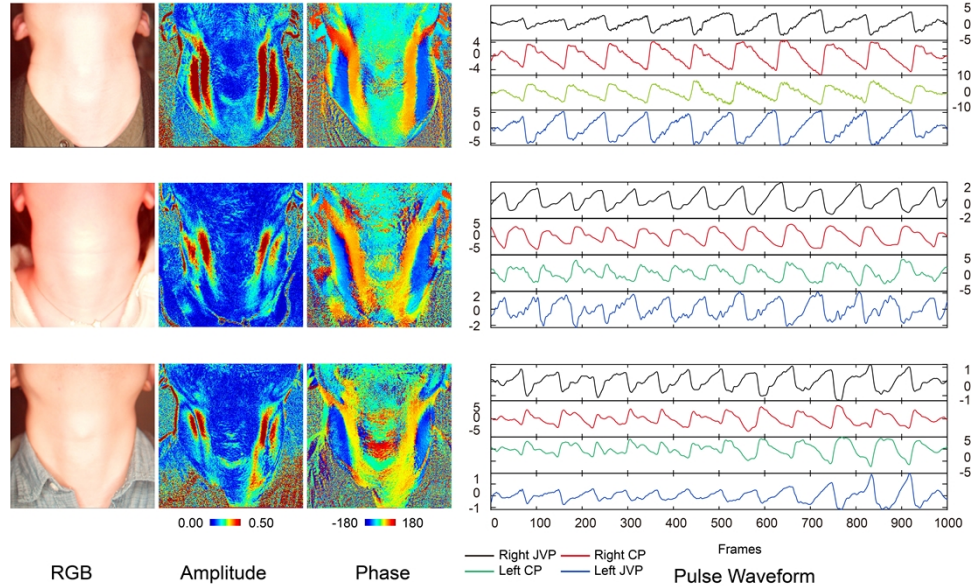

Fig. 4. Extraction of JVP and CP waveform from three example subjects. In these three cases: amplitude maps show four distinct linear regions with high motion amplitudes are located at the two sides of necks, indicating clear leading and delay phases; extracted CP waves consists of systolic peaks and dicrotic notches; most JVP waveform contain positive "a", "c", "v" and negative "x", "y" waves. Photos on the left are shown for reference and represent one frame in the recorded video by the camera.

To evaluate the accuracy of the measurements in estimating the JVP and CP waveforms, we conducted a comparison between the measurements and a standard waveform obtained from a previous study [28], as illustrated in Fig. 5(a). The standard waveform was obtained using contact photoplethysmography with the assistance of infrared imaging. Figure 5(b) presents the calculated centroids of the standard CP and JVP waveforms. In Fig. 5(c), we computed the centroid of the extracted pulse waveforms and compared them with the standard data. Each mask region included nine subjects, with ten pulse periods measured for each subject. To account for individual differences, such as heart rate, we compared the extracted waveforms within cardiac cycles rather than using absolute timing. The results reveal that the centroid measured from region cmask_2 (right CP region) and cmask_3 (left CP region) closely matches the position of the standard CP centroid, while the centroid measured from region cmask_1 (right JVP region) and cmask_4 (left JVP region) aligns with the position of the standard JVP centroid. This observation indicates that our method can successfully extract pulse waveforms with distinct morphological features. Figure 5(d) presents the quantification of correlation coefficients between the standard and extracted pulse waveforms. The results were summarized from nine subjects. Our findings indicate that pulse waveforms extracted from regions cmask_1 and cmask_4 of the composite mask display moderate correlations (0.66 and 0.68, respectively, $p < 0.001$) with CP waveforms, while those from regions cmask_2 and cmask_3 demonstrate higher correlations (0.76 and 0.73,

respectively, p < 0.001) with JVP waveforms. This suggests that the measurements reasonably represent the CP and JVP waveforms. Additionally, we investigated the phase relationship between the extracted JVP and CP waveforms. We calculated the phase differences between CP and JVP on the right side (regions cmask_2 and cmask_1) and left side (regions cmask_3 and cmask_4) for each subject, which are given in Fig. 5(e). The graph shows that the extracted JVP and CP waveforms exhibit a relative reversed phase for each subject.
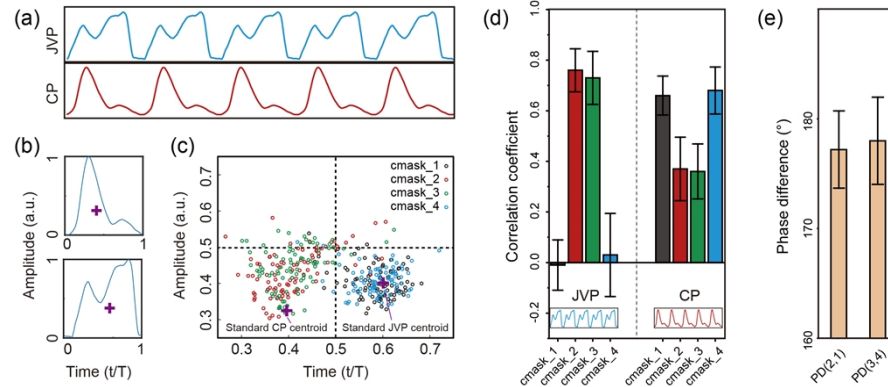

Fig. 5. Evaluation of extracted pulse waveforms. (a) Standard JVP and CP waveforms from previous study. (b) Calculation of centroids of standard CP and JVP waveforms. The centroids of the standard CP and JVP waveforms are calculated and labeled with a purple cross. (c) Comparison of centroids between extracted and standard pulse waveforms: The centroids of various extracted pulse waveforms are compared with the standard waveforms. The positions of the extracted pulse waveforms are labeled with circles in four different colors, corresponding to four original mask regions. Centroids were extracted from 90 pulse periods of nine subjects for each region. (d) Correlation coefficients between standard and extracted pulse waveforms. The correlation coefficients between the standard waveforms and the pulse waveforms extracted from composite mask regions (cmask_1 to cmask_4: the left to right regions in Fig. 3(d)) are calculated. The pulse waveforms were calculated for all nine subjects. (e) Phase difference between extracted JVP and CP. The phase difference between the extracted JVP and CP waveforms is measured in both the left and right sides. The phase difference between pulse waveforms extracted from composite mask regions 3 and 4 is denoted as PD (3, 4), whereas the phase difference between pulse waveforms extracted from composite mask regions 2 and 1 is denoted as PD (2, 1).

4.   Discussions

We described a µMI method to provide non-contact measurements of CP and JVP waves. Experimental results demonstrated the feasibility of this method to directly acquire, differentiate and analyze pulse waves in a non-contact and non-invasive manner. More importantly, the proposed approach is highly self-efficient in data acquisition and processing, which can be independently operated without needed additional support. For example, the amplitude and phase maps are self-derived from the video. In addition, CP and JVP waveforms are extracted from the recorded videos under the guidance of self-derived phase maps. Therefore, with a simple device setup without a need for an expert to operate, this technique is more easily accessible by the public in their daily lives. This attribute would be extremely useful in the development of methods (either diagnostic or predictive) to prevent and/or early screen cardiovascular diseases, especially carotid stenosis.

In a previous study, we developed a smartphone-enabled imaging PPG (iPPG) system to measure blood pulsation of the circulating blood volume within the light interrogated skin tissue

beds [32,33]. Similar to the purpose in the current study, this prior study also acquired signals from skin reflections and extracted regional pulsations. Several studies have employed various post-processing algorithms to refine pulse signals obtained from webcams or consumer cameras [34–39]. However, these prior techniques primarily focused on detecting blood pulsation through light absorption variation in tissue beds. In contrast, our µMI approach was specifically developed to capture tissue motions due to the pulsation in CA and JV at the neck region. As illustrated in Fig. 2, motion-induced signals exhibit significantly stronger pulsation amplitudes. Importantly, unlike previous iPPG studies that measured signals from distal capillary beds, µMI enables direct access to CA and JV information, facilitating a more straightforward assessment of cardiovascular functions. Some other studies have made adjustments to access signals from larger blood vessels, such as employing near-infrared light sources to enhance penetration depth [40,41]. However, these modifications often require higher investment for developing the technique. While our study aligns with the underlying principles of previous works by Yong et al. [42], HajiRassouliha et al. [43], and Douplik et al. [44,45] where motion-modulated reflection images were used to extract pressure pulse signals, we have developed an improved strategy to implement the methodology. Notably, compared with HajiRassouliha's and Yong's methods, the proposed strategy provides self-guidance to automatically identify the JVP and CP regions. Compared to Douplik's approach, our method eliminates the need for manual identification of pulsation regions, thereby simplifying the procedure and minimizing the subjectiveness in the measurements. Furthermore, by utilizing a composite mask that integrates intensity and phase information, our approach enables more accurate identification of blood vessels. This proposed methodology not only facilitates signal extraction from carotid arteries and jugular veins using neck skin but also provides criteria for distinguishing between different types of blood vessels, potentially improving the accuracy and reliability of the analysis. Contact PPG approaches can also be devised to directly measure the heart pulse waveform. However, as we presented above, JVs and common CA are closely located, which can easily cause inaccurate positioning of the sensor probe, leading to a severe distortion of waveform. An alternative would be to position the sensor probe under the guidance of other techniques, which would cause additional complexity and operation costs. Compared with these techniques, our µMI system and method provide more direct and accurate assessments with better usability.

To demonstrate the feasibility of our method in measuring JVP and CP waveforms, we conducted a correlation analysis between our measurements and standard pulse waveforms obtained through contact PPG. The correlation coefficient serves as an indicator of the similarity between the measured pulse waveform and the standard. However, several factors can limit the correlation between the two measurements. Firstly, JVP and CP waveforms exhibit high individual variability due to various psychological and health factors, which could underscore their diagnostic potential. Secondly, the differences in measurements likely contribute to the degradation of correlation that we observed in this study. Here, our µMI system used a contactless mode to capture mechanical tissue movements, whereas the standard waveforms were derived from absorption changes through contact measurement. Consequently, the correlation tends to remain moderate to high, rather than approaching higher levels. One way to address this limitation is to conduct an optimized correlation analysis between two measurements from the same individual. Another approach could involve training a deep learning model to facilitate waveform reconstruction between the two modalities, potentially leading to closer resemblance to contact PPG waveforms.

There are some limitations when using µMI to measure and analyze the CP and JVP waveform from the neck region. Even though a 16-bit camera was employed in our current development, low light-tissue interaction efficiency and uncontrolled relative motions between the system and skin may impose a practical challenge in the data acquisition to guarantee the signal with sufficient signal quality. Besides, as a proof-of-concept study, we imaged and analyzed a relatively small

sample set, the participants recruited in this study also lack diversity in age and health conditions. It is likely that the performance of this proposed method will be challenged when imaging patients with real cardiovascular diseases in clinical settings. In future, we will keep working on the post-processing method to improve the signal quality of acquired pulse waveform. Meanwhile, we will apply the proposed system and method in clinical imaging for further refinements and optimizations.

5. Conclusions

We have reported an μMI system and method to measure neck pulse waves from the micro-motions in the neck skin. A 16-bit camera was equipped in the system to record pulsatile motions with high fidelity. Lock-in amplification algorithm was used to derive the amplitude and phase of heart-cycle-related pulsatile motions to generate composite masks. Guided by these masks, we extracted CP and JVP waveform from the acquired skin videos. While the method and proposed strategy require further refinement in order to achieve robust measurements of CP and CVP waveforms in live subjects, the preliminary experimental results presented here does demonstrate that our method is feasible to extract CP and JVP waveforms in a non-contact manner. Furthermore, since the measurement can be realized by simply recording a video of neck skin, it is easy to use without a need of an expert to operate, which can be accessed by the general public as an early screening tool for potential cardiovascular diseases.

Disclosures. The authors declare no conflict of interest at the current stage of development.

Data availability. Data underlying the results presented in this paper are not publicly available at this time but may be obtained from the authors upon reasonable request.

References

1. H. Wang, M. Naghavi, C. Allen, R. M. Barber, Z. A. Bhutta, A. Carter, D. C. Casey, F. J. Charlson, A. Z. Chen, and M. M. Coates, "Global, regional, and national life expectancy, all-cause mortality, and cause-specific mortality for 249 causes of death, 1980–2015: a systematic analysis for the Global Burden of Disease Study 2015," The Lancet **388**(10053), 1459–1544 (2016).
2. GBD Mortality and Causes of Death Collaborators, "Global, regional, and national age-sex specific all-cause and cause-specific mortality for 240 causes of death, 1990-2013: a systematic analysis for the Global Burden of Disease Study 2013," Lancet **385**(9963), 117–171 (2015).
3. G. Mowatt, J. A. Cook, G. S. Hillis, S. Walker, C. Fraser, X. Jia, and N. Waugh, "64-Slice computed tomography angiography in the diagnosis and assessment of coronary artery disease: systematic review and meta-analysis," Heart **94**(11), 1386–1393 (2008).
4. A. Knez, C. R. Becker, A. Leber, B. Ohnesorge, A. Becker, C. White, R. Haberl, M. F. Reiser, and G. Steinbeck, "Usefulness of multislice spiral computed tomography angiography for determination of coronary artery stenoses," Am. J. Cardiol. **88**(10), 1191–1194 (2001).
5. J. A. C. Lima and M. Y. Desai, "Cardiovascular magnetic resonance imaging: current and emerging applications," J. Am. Coll. Cardiol. **44**(6), 1164–1171 (2004).
6. C. M. Kramer, J. Barkhausen, S. D. Flamm, R. J. Kim, and E. Nagel, "Standardized cardiovascular magnetic resonance imaging (CMR) protocols, society for cardiovascular magnetic resonance: board of trustees task force on standardized protocols," J. Cardiovasc. Magn. Reson. **10**(1), 35 (2008).
7. J. Thiruvengadam, M. Anburajan, M. Menaka, and B. Venkatraman, "Potential of thermal imaging as a tool for prediction of cardiovascular disease," J. Med. Phys. **39**(2), 98–105 (2014).
8. M. Garbey, N. Sun, A. Merla, and I. Pavlidis, "Contact-free measurement of cardiac pulse based on the analysis of thermal imagery," IEEE Trans. Biomed. Eng. **54**(8), 1418–1426 (2007).
9. M. K. Shourav, S. Salsabila, J.-Y. Lee, and J. K. Kim, "Estimation of core body temperature by near-infrared imaging of vein diameter change in the dorsal hand," Biomed. Opt. Express **12**(8), 4700–4712 (2021).
10. G. J. Ughi, H. Wang, E. Gerbaud, J. A. Gardecki, A. M. Fard, E. Hamidi, P. Vacas-Jacques, M. Rosenberg, F. A. Jaffer, and G. J. Tearney, "Clinical characterization of coronary atherosclerosis with dual-modality OCT and near-infrared autofluorescence imaging," JACC: Cardiovascular imaging **9**, 1304–1314 (2016).
11. L. C. de Vos, D. J. Mulder, A. J. Smit, R. P. F. Dullaart, N. Kleefstra, W. M. Lijfering, P. W. Kamphuisen, C. J. Zeebregts, and J. D. Lefrandt, "Skin autofluorescence is associated with 5-year mortality and cardiovascular events in patients with peripheral artery disease," Arterioscler., Thromb., Vasc. Biol. **34**(4), 933–938 (2014).
12. S. Zaunseder, A. Trumpp, D. Wedekind, and H. Malberg, "Cardiovascular assessment by imaging photoplethysmography–a review," Biomed. Tech. **63**(5), 617–634 (2018).

13. J. H. Lam, K. J. Tu, J. Kim, and S. Kim, "Smartphone-based single snapshot spatial frequency domain imaging," Biomed. Opt. Express **13**(12), 6497–6507 (2022).

14. J. Jiang, A. D. C. Mata, S. Lindner, E. Charbon, M. Wolf, and A. Kalyanov, "2.5 Hz sample rate time-domain near-infrared optical tomography based on SPAD-camera image tissue hemodynamics," Biomed. Opt. Express **13**(1), 133–146 (2022).

15. A. Garrett, B. Kim, E. J. Sie, N. Z. Gurel, F. Marsili, D. A. Boas, and D. Roblyer, "Simultaneous photoplethysmography and blood flow measurements towards the estimation of blood pressure using speckle contrast optical spectroscopy," Biomed. Opt. Express **14**(4), 1594–1607 (2023).

16. B. Lee, O. Sosnovtseva, C. M. Sørensen, and D. D. Postnov, "Multi-scale laser speckle contrast imaging of microcirculatory vasoreactivity," Biomed. Opt. Express **13**(4), 2312–2322 (2022).

17. Z. Ovadia-Blechman, I. Avrahami, E. Weizman-Shammai, T. Sharir, M. Eldar, and P. Chouraqui, "Peripheral microcirculatory hemodynamic changes in patients with myocardial ischemia," Biomed. Pharmacother. **74**, 83–88 (2015).

18. F. Lapostolle, P. Le Toumelin, J. M. Agostinucci, J. Catineau, and F. Adnet, "Basic cardiac life support providers checking the carotid pulse: performance, degree of conviction, and influencing factors," Acad. Emerg. Med. **11**(8), 878–880 (2004).

19. M. M. Applefeld, "The jugular venous pressure and pulse contour," Clinical methods: The history, physical, and laboratory examinations **107**, 1 (1990).

20. N. Ranganathan, V. Sivaciyan, and F. B. Saksena, "Local and systemic manifestations of cardiovascular disease," in *The art and science of cardiac physical examination* (Springer, 2006), pp. 361–395.

21. S. Parittotokkaporn, D. de Castro, A. Lowe, and R. Pylypchuk, "Carotid Pulse Wave Analysis: Future Direction of Hemodynamic and Cardiovascular Risk Assessment," JMA J **4**(2), 119–128 (2021).

22. H. K. Walker, W. D. Hall, and J. W. Hurst, "Clinical methods: the history, physical, and laboratory examinations," (1990).

23. M. H. Drazner, J. E. Rame, L. W. Stevenson, and D. L. Dries, "Prognostic importance of elevated jugular venous pressure and a third heart sound in patients with heart failure," N. Engl. J. Med. **345**(8), 574–581 (2001).

24. S. R. Mittal, S. Garg, and M. Lalgarhia, "Jugular venous pressure and pulse wave form in the diagnosis of right ventricular infarction," Int. J. Cardiol. **53**(3), 253–256 (1996).

25. R. W. Taylor and A. V. Palagiri, "Central venous catheterization," Crit. Care Med. **35**(5), 1390–1396 (2007).

26. P. Zamboni, "Why current Doppler ultrasound methodology is inaccurate in assessing cerebral venous return: the alternative of the ultrasonic jugular venous pulse," Behav. Neurol. **2016**, 1–7 (2016).

27. X. Li, J. Jiang, H. Zhang, H. Wang, D. Han, Q. Zhou, Y. Gao, S. Yu, and Y. Qi, "Measurement of carotid pulse wave velocity using ultrafast ultrasound imaging in hypertensive patients," J. Med. Ultrasonics **44**(2), 183–190 (2017).

28. I. García-López and E. Rodriguez-Villegas, "Extracting the jugular venous pulse from anterior neck contact photoplethysmography," Sci. Rep. **10**(1), 3466 (2020).

29. J. Park, B. Park, J. Ahn, D. Kim, J. Y. Kim, H. H. Kim, and C. Kim, "Opto-ultrasound biosensor for wearable and mobile devices: realization with a transparent ultrasound transducer," Biomed. Opt. Express **13**(9), 4684–4692 (2022).

30. T. Boonya-Ananta, A. J. Rodriguez, V. N. Du Le, and J. C. Ramella-Roman, "Monte Carlo analysis of optical heart rate sensors in commercial wearables: the effect of skin tone and obesity on the photoplethysmography (PPG) signal," Biomed. Opt. Express **12**(12), 7445–7457 (2021).

31. J. Yan, Z. Ye, F. Shi, Y. Dai, L. Yang, J. Wu, and Y. Wang, "Reflection-type photoplethysmography pulse sensor based on an integrated optoelectronic chip with a ring structure," Biomed. Opt. Express **12**(10), 6277–6283 (2021).

32. Q. He, Z. Sun, Y. Li, W. Wang, and R. K. Wang, "Spatiotemporal monitoring of changes in oxy/deoxy-hemoglobin concentration and blood pulsation on human skin using smartphone-enabled remote multispectral photoplethysmography," Biomed. Opt. Express **12**(5), 2919–2937 (2021).

33. Z. Sun, Q. He, Y. Li, W. Wang, and R. K. Wang, "Robust non-contact peripheral oxygenation saturation measurement using smartphone-enabled imaging photoplethysmography," Biomed. Opt. Express **12**(3), 1746–1760 (2021).

34. H. Gao, C. Zhang, S. Pei, and X. Wu, "LSTM-based real-time signal quality assessment for blood volume pulse analysis," Biomed. Opt. Express **14**(3), 1119–1136 (2023).

35. A. K. Maity, J. Wang, A. Sabharwal, and S. K. Nayar, "RobustPPG: camera-based robust heart rate estimation using motion cancellation," Biomed. Opt. Express **13**(10), 5447–5467 (2022).

36. A. A. Kamshilin, S. Miridonov, V. Teplov, R. Saarenheimo, and E. Nippolainen, "Photoplethysmographic imaging of high spatial resolution," Biomed. Opt. Express **2**(4), 996–1006 (2011).

37. G. Xu, L. Dong, J. Yuan, Y. Zhao, M. Liu, M. Hui, Y. Zhao, and L. Kong, "Rational selection of RGB channels for disease classification based on IPPG technology," Biomed. Opt. Express **13**(4), 1820–1833 (2022).

38. S. Borik, P. Procka, J. Kubicek, and C. H. Antink, "Skin tissue perfusion mapping triggered by an audio-(de) modulated reference signal," Biomed. Opt. Express **13**(7), 4058–4070 (2022).

39. E. M. Nowara, D. McDuff, and A. Veeraraghavan, "Systematic analysis of video-based pulse measurement from compressed videos," Biomed. Opt. Express **12**(1), 494–508 (2021).

40. D. Cheng, J. Wang, T. Yokota, and T. Someya, "Spatiotemporal processing in photoplethysmography for skin microcirculatory perfusion imaging," Biomed. Opt. Express **13**(2), 838–849 (2022).

41. R. Amelard, A. D. Robertson, C. A. Patterson, H. Heigold, E. Saarikoski, and R. L. Hughson, "Optical hemodynamic imaging of jugular venous dynamics during altered central venous pressure," IEEE Trans. Biomed. Eng. **68**(8), 2582–2591 (2021).
42. F. Abnousi, G. Kang, J. Giacomini, A. Yeung, S. Zarafshar, N. Vesom, E. Ashley, R. Harrington, and C. Yong, "A novel noninvasive method for remote heart failure monitoring: the EuleriAn video Magnification apPLications In heart Failure studY (AMPLIFY)," Npj Digit. Med. **2**(1), 80 (2019).
43. E. J. Lam Po Tang, A. HajiRassouliha, M. P. Nash, P. M. F. Nielsen, A. J. Taberner, and Y. O. Cakmak, "Non-contact quantification of jugular venous pulse waveforms from skin displacements," Sci. Rep. **8**(1), 17236 (2018).
44. T. Burton, G. Saiko, and A. Douplik, "Towards development of specular reflection vascular imaging," Sensors **22**(8), 2830 (2022).
45. G. Saiko, T. Burton, and A. Douplik, "Feasibility of specular reflection imaging for extraction of neck vessel pressure waveforms," Front. Bioeng. Biotechnol. **10**, 406 (2022).